Cold Sintering Halide-in-Oxide Composite Solid-State Electrolytes with Enhanced Ionic Conductivity

Bo Nie[1], Ta-Wei Wang[1], and Hongtao Sun[1,2*]

[1]The Harold & Inge Marcus Department of Industrial & Manufacturing Engineering, Pennsylvania State University, University Park, PA, USA. [2]Materials Research Institute (MRI), Pennsylvania State University, University Park, PA, USA

[*]Corresponding authors: hongtao.sun@psu.edu (H. Sun)

Abstract

All-solid-state batteries (ASSBs) have attracted increasing attention for next-generation electrochemical energy storage owing to their high energy density and enhanced safety, achieved through the use of non-flammable solid-state electrolytes (SSEs). Oxide-based SSEs, such as $Li_{1.3}Al_{0.3}Ti_{1.7}(PO_4)_3$ (LATP), are notable for their high ionic conductivity and excellent chemical and electrochemical oxidation stability. Nevertheless, their brittle mechanical properties and poor interface contact with electrode materials necessitate high-temperature and long-duration sintering or post calcination processes, limiting their processability for real-world applications. Additionally, the formation of secondary phases can detrimentally affect the ionic conductivity of LATP electrolytes. Emerging halide-based SSEs offer reliable deformation for practical processing while maintaining high ionic conductivity. In this work, we report a transient liquid-assisted cold sintering process to integrate oxide-based LATP as the matrix and halide-based Li_3InCl_6 as the conductive boundary phase into a halide-in-oxide ceramic composite electrolyte at a low processing temperature of 150 ℃. This composite structure significantly reduces interface resistance, effectively addressing ion transport depletion across the boundaries between LATP particles. Consequently, the co-sintered LATP-Li_3InCl_6 composite SSE exhibits high ionic conductivity of 1.4×10^{-4} S cm^{-1} at ambient temperature. Furthermore, the symmetric Li|LATP-$Li_3InCl_6 \cdot n$DMF|Li cell demonstrates stable stripping and plating processes for 1600 hours at 55 ℃ (0.1 mA cm^{-2}) and 1200 hours at 100 ℃ (1 mA cm^{-2}). This work represents the first demonstration of ceramic-in-ceramic SSEs that combine the advantages of oxides and halides for high-performance SSBs.

Introduction

Conventional Li-ion batteries with liquid electrolytes offer good performance due to the high conductivity and excellent wetting of the electrode surfaces provided by the electrolyte solutions [1]. However, the flammable liquid organic solvents pose drawbacks, including stability issues and safety concerns [2–8]. In contrast, all-solid state batteries (ASSBs) not only attenuate these issues by offering higher electrochemical and thermal stabilities but also provide higher energy density [8–16]. Owing to these benefits, research on solid-state electrolytes (SSEs) has rapidly expanded in recent years.

Among SSEs, inorganic solid-state electrolytes have attracted considerable attention because of their outstanding thermal stability, wide electrochemical window, and superior mechanical properties (to block dendrite growth). For example, inorganic SSEs can support battery operation at temperatures as low as -50°C and as high as 200°C [17]. Inorganic SSEs have been widely investigated, including oxide-based (*e.g.*, perovskite-type $Li_{0.33}La_{0.557}TiO_3$, LISICON-type $Li_{3.75}Ge_{0.75}P_{0.25}O_4$ [18,19], NASICON-type $Li_{1+x}Al_xTi_{2-x}(PO_4)_3$, and garnet-type $Li_7La_3Zr_2O_{12}$) [18–26], sulfide-based (*e.g.*, Li_2S-P_2S_5 and Li_2S-P_2S_5-MS_x) [18], and halide-based (*e.g.*, Li_3InCl_6) [27], and polymer-inorganic composite-based SSEs [28].

$Li_{1+x}Al_xTi_{2-x}(PO_4)_3$ (LATP) is distinguished for its decent ionic conductivities, ranging from 10^{-3}–10^{-4} S cm^{-1} at room temperature, as well as its excellent chemical and electrochemical oxidation stability in air. LATP consists of $LiTi_2(PO_4)_3$ (LTP) with a NASICON structure, where Ti^{4+} ions are partially substituted with Al^{3+} ions. The TiO_6 octahedra and PO_4 tetrahedra in LTP form a three-dimensional network, creating cavities that accommodate Li^+ ions [29]. The substitution with Al^{3+} ions reduces unit cell dimensions and promotes densification, thereby enhancing ionic conductivity.

The synthesis method significantly influences the conductivity of LATP SSEs. These methods can be categorized into solid-based and liquid-based approaches. Solid-based approaches, such as the sintering processes, require high temperatures (700 -1200°C) and prolonged dwell times (over 12 hours) to achieve complete solid-state reactions and high densification [30–34]. On the other hand, liquid-based approaches, including sol-gel, and coprecipitation methods, combined with post-calcination [35,36], often yield more uniform particle distribution and homogeneous microstructure. However, both approaches face issues related to secondary phase formation at grain boundaries, which

can adversely affect ionic conductivity. For example, $AlPO_4$ commonly forms an amorphous barrier layer at the grain boundaries of LATP [37]. Additionally, the brittle mechanical properties of LATP and its poor interface contact with electrode materials limit its performance and processability for real-world applications.

The cold sintering process (CSP) is an energy and time-efficient method that uses transient liquid as sintering aid [38]. This process consolidates ceramic and ceramic composite SSEs at low sintering temperatures through a dissolution-precipitation-creep mechanism. The low processing temperature allows for readily manipulation of compositions, structures, and properties at interfacial boundaries, resulting in improved ionic conductivity across these boundaries. For instance, lithium salts such as LiTFSI and $LiClO_4$, when dissolved in transient liquids, have proven effective as sintering aids, significantly enhancing the ionic conductivity of grain boundaries in oxide-based electrolytes [39]. Kim et al. utilized a Dimethylformamide (DMF) and H_2O mixture as a transient solvent to control the dissolution-precipitation of dissolved LiTFSI at local grain boundaries during CSP, achieving a high ionic conductivity of 1.65×10^{-4} S cm^{-1} [40]. Moreover, integrating ionically conducting polymers as the grain boundary phase with a ceramic electrolyte matrix to form polymer-in-ceramic composite SSEs can dramatically reduce interface resistance but compromise ceramic electrolyte's wide voltage window and high thermal stability [28,41,42].

In this work, we report a transient liquid-assisted CSP to integrate oxide-based LATP as the matrix and halide-based Li_3InCl_6 as the conductive boundary phase into a halide-in-oxide ceramic composite electrolyte at a low processing temperature of 150 °C. Unlike previously reported polymer-in-ceramic composite SSEs, the halide-based ionic conducting phase, which possesses excellent mechanical deformability, not only reduces interface resistance and addresses ion transport depletion across the boundaries between LATP particles but also maintains the advantage of ceramic SSEs, including high thermal and chemical stability and wide voltage windows. Consequently, the co-sintered LATP-Li_3InCl_6 composite electrolyte exhibits high ionic conductivity of 1.4×10^{-4} S cm^{-1} at ambient temperature. This work represents the first demonstration of ceramic-in-ceramic SSEs that combine the advantages of oxides and halides for high-performance ASSBs.

Experimental methods

Fabrication of LATP-Li$_3$InCl$_6$·nDMF composite SSEs. Li$_3$InCl$_6$-based halide was introduced as a microstructural boundary phase to reduce the interface resistance and enhance the ionic conductivity of LATP-Li$_3$InCl$_6$ composite SSEs. Commercial LATP powders (MSE Supplies Inc.) with a particle size of 1-5 μm were used as received without any modification. LiCl ($\geq$99.98% trace metals, Sigma) and InCl$_3$ (98%, Sigma) precursors, in a 3:1 molar ratio, were dissolved in water to form the solution. LATP was then mixed with varying amounts of the synthesized halide (10, 15, 20, and 25 wt% of halide content) to create an evenly dispersed mixture. After water evaporation, the powders were heat-treated at 260 ℃ under vacuum for 4 hours to remove coordinated water in Li$_3$InCl$_6$·H$_2$O. The composite powders were transferred to a glovebox and further mixed with a small amount of Dimethylformamide (DMF, anhydrous, Sigma) using a mortar and pestle. The CSP was conducted at different temperatures (90, 120, 150, and 200 ℃) for 60 min with a heating rate of 10 ℃ min^{-1}. Due to relatively low sintering temperature and time, a trivial amount of DMF may remain in the composite electrolyte as ligands of the metal ions (i.e. In(III)) [43]. The obtained composite SSE is labeled as LATP-Li$_3$InCl$_6$·nDMF.

Material Characterization. The morphological and structural characteristics were analyzed using scanning electron microscopy (SEM, Thermoscientific Verios G4) and X-ray diffraction (XRD) (Panalytical Empyrean 3 Powder Diffractometer).

In-situ Electrochemical Impedance Spectroscopy (EIS) monitoring. The cold sintering die was modified with a boron nitride (BN) sleeve and two leads welded at the upper and lower die terminals. In-situ EIS (Ametek, Princeton Applied Research, Versa STAT 4) were performed with a sinusoidal signal in a frequency range from 100 kHz to 100 Hz at an amplitude of 100 mV at specific temperatures throughout the CSP.

Electrochemical Measurements. The ionic conductivity of the prepared composite SSEs was measured between two stainless steel (SS) blocking electrodes using EIS at open circuit potential, with a sinusoidal signal in a frequency range from 100 kHz to 10 mHz at an amplitude of 10 mV. The symmetric cell test was conducted by assembling the prepared composite SSEs between two thin Li disks (100μm) and evaluated in a DC cycling test (Landt Instrument). The stripping and platting were conducted at current densities of 0.02, 0.05, 0.1, 0.2, 0.5, 1 mA cm^{-2}, and back to 0.1 mA cm^{-2} for 1 hour at

55 ℃, respectively. The stripping and platting cycling test with the areal capacity of 1 mAh cm^{-2} and a current density of 1 mA cm^{-2} was further tested at 100 ℃.
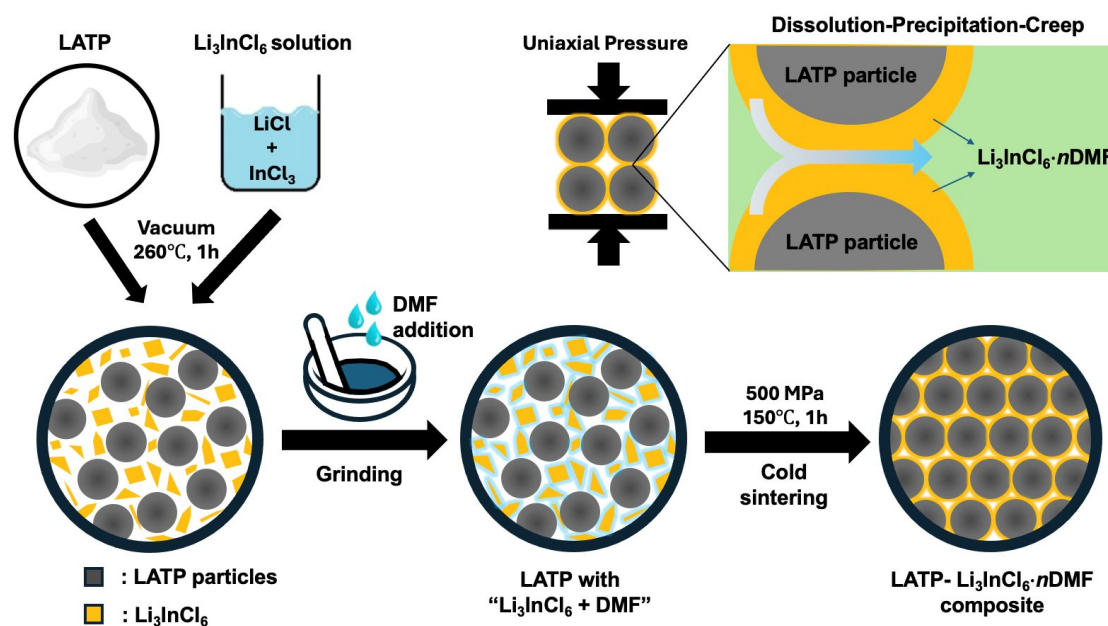

Figure 1. Schematic of the fabrication process for LATP-Li$_3$InCl$_6$·nDMF composite SSE.

Result and discussion

Figure 1 shows the whole fabrication process and CSP of the LATP-Li$_3$InCl$_6$·nDMF composite electrolyte. The dissolution-precipitation-creep mechanism leads to the formation of Li$_3$lnCl$_6$·nDMF boundary phase coating on the surface of LATP particles [44]. During densification, Li$_3$lnCl$_6$ dissolves in the DMF solvent and diffuses into the voids and empty spaces between LATP particles. As the temperature increases, the DMF gradually evaporates and escapes from the semi-open system. Under both the pressure and heat, the halide salts precipitate on the surfaces of LATP particles, occupying the empty spaces. The microstructure of the co-sintered composite electrolyte was studied using scanning electron microscopy (SEM). SEM images of the cross-sectional view of the fractured LATP-Li$_3$InCl$_6$·nDMF composite sintered at 150 ℃ are shown in Figure 2a and 2b. The particles densified into a composite pellet still exhibit a porosity of approximately 16%. As shown in the inset of Figure 2b, the Li$_3$InCl$_6$·nDMF halide phase coats precipitated on the surface of LATP particles and within inter-particle voids, creating interconnected lithium-ion diffusion pathway. The

uniform distribution of the Li_3InCl_6 phase is further confirmed by element mapping via energy dispersive spectroscopy (EDS) (Figure 2c and 2d), where Cl and In are evenly distributed in a relatively higher concentration between the LATP particles.
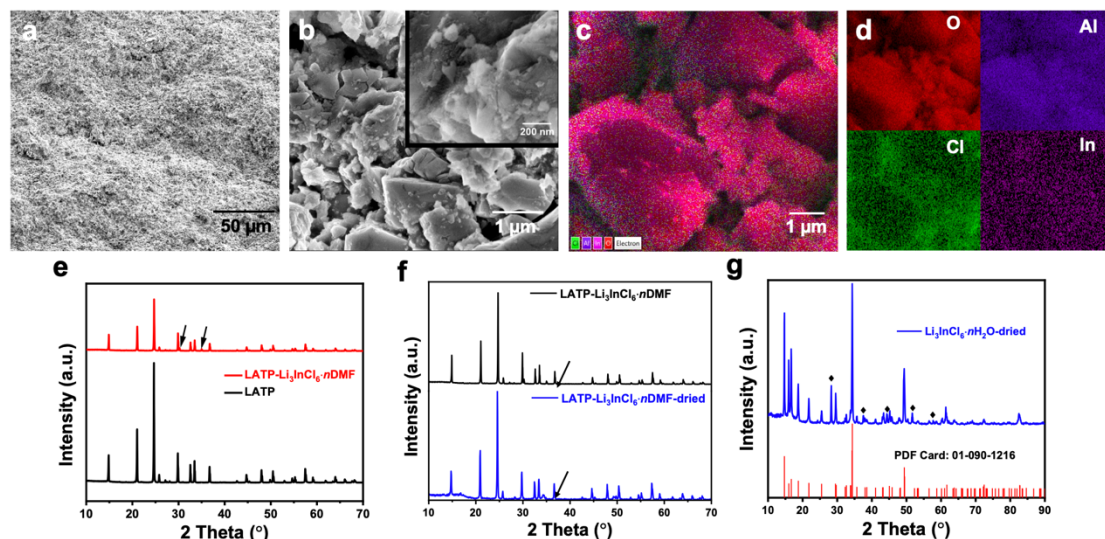

Figure 2. Material characterizations of the LATP-Li₃InCl₆·_n_DMF composite electrolyte cold sintered at 150°C. (a,b) SEM images, **(c,d)** EDS images, **(e)** XRD pattern of LATP-Li₃InCl₆·_n_DMF composite compared to LATP, **(f)** XRD pattern of LATP-Li₃InCl₆·_n_DMF compared to vacuum-dried sample, and **(g)** XRD pattern of vacuum-dried Li₃InCl₆·_n_H₂O.

As mentioned in the Experimental Method section, due to the presence of trace DMF in the composite electrolyte acting as ligands with In (III), the fabricated composite electrolyte with the halide phase of $Li_3InCl_6 \cdot n$DMF was studied by X-ray diffraction (Figure 2e). Compared with the pure LATP powder, the composite electrolyte exhibited additional peaks that were neither characteristics of LiCl nor $InCl_3$. Furthermore, the composite electrolyte was vacuum dried at 260 °C for 4h. As shown in Figure 2f, the X-ray diffraction pattern showed an impurity peak shift from 35.0° to 34.3°, corresponding to the indexed peak of vacuum-dried $Li_3InCl_6 \cdot n$H$_2$O and the reported Li_3InCl_6 (PDF:01-090-1216) (Figure 2g). However, the vacuum-dried LATP-$Li_3InCl_6 \cdot n$DMF composite exhibited much larger resistance compared to the LATP-$Li_3InCl_6 \cdot n$DMF composite itself (Figure S1). This increased resistance could be due to the contribution of DMF to the bonding between the halide phase and LATP particles. Additionally, the DMF ligands may provide an extra Li^+ diffusion pathway throughout
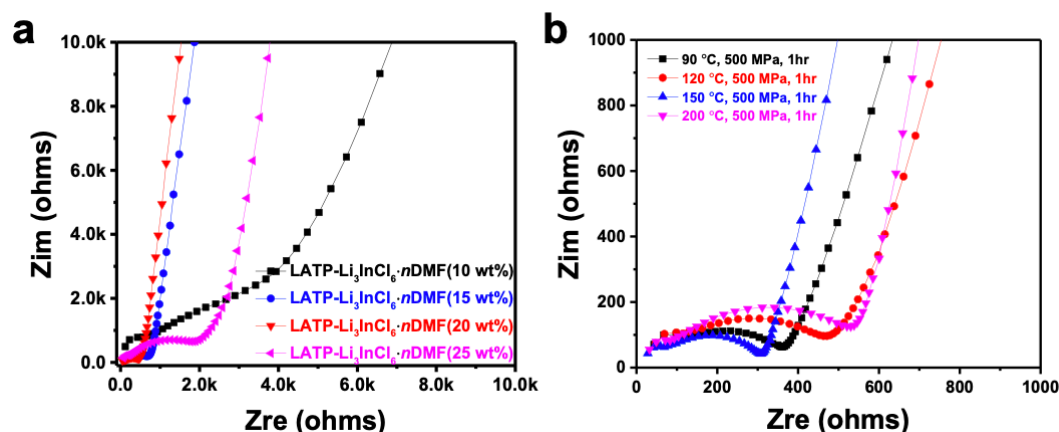
the densified electrolyte material.

Figure 3. The Nyquist plot of the LATP-Li$_3$InCl$_6$·nDMF composite electrolyte with different content ratios (a), sintering temperatures (b).

To investigate the effect of incorporating Li$_3$InCl$_6$·nDMF halide into LATP, we co-sintered LATP-Li$_3$InCl$_6$·nDMF with different halide contents at a cold sintering temperature of 150 ℃ (much lower than the solid-state sintering temperature of LATP). The EIS measurements on these LATP-Li$_3$InCl$_6$·nDMF composite electrolytes at 25 ℃ are presented in Figure 3a. The results indicate that the grain boundary contribute dominantly to the total conductivity, with a specific amount of halide (20 wt%) presenting the smallest resistance. Both low (10 wt%) and high halide contents (25 wt%) led to large resistance. We speculate that the reduced resistance at 20 wt% is mainly due to the optimized occupation of seams by the halide phase, bridging the LATP micro-sized particles and effectively reducing the interface resistance.

To evaluate the process parameters, various sintering temperatures were analyzed for their impact on resistances (Figure 3b). Herein, LATP-Li$_3$InCl$_6$·nDMF (20 wt% halide) was sintered at 90, 120, 150, and 200 ℃ under 500MPa pressure for 1 hour. Interestingly, the composite solid electrolyte exhibited the largest resistance at the highest sintering temperature of 200 ℃. In solvent chemistry, the DMF solvato ligands in InCl$_3$-based inorganic transformations (InCl$_3$(dmf)$_2$) may act as a chemical reagents and induce the formation of [In(CO$_2$R)$_4$] − at higher temperature [43,45]. This ~~coordination~~ phenomenon might happen during the 200 ℃ sintering process and hinder the ion transportation inside the composite electrolyte. At the lower temperature

of 90 °C, the composite electrolyte, containing DMF, forms a system that reduces resistance through ion solvation due to the remaining liquid DMF. As the sintering temperature increases to 150 °C, the co-sintered composite electrolyte exhibited the lowest resistance, likely due to the more efficient dissolution-evaporation-precipitation process for DMF-driven boundary phase formation in the system. Additionally, heat treatment at 150 °C for 1 hour evaporated most of the DMF solvent, resulting in an all-solid-state composite electrolyte with only a trace amount of DMF. In-situ EIS measurements conducted at different temperatures during the heating and cooling processes (Figure S2) showed that higher temperatures resulted in lower resistance, following the modified Arrhenius law [46].
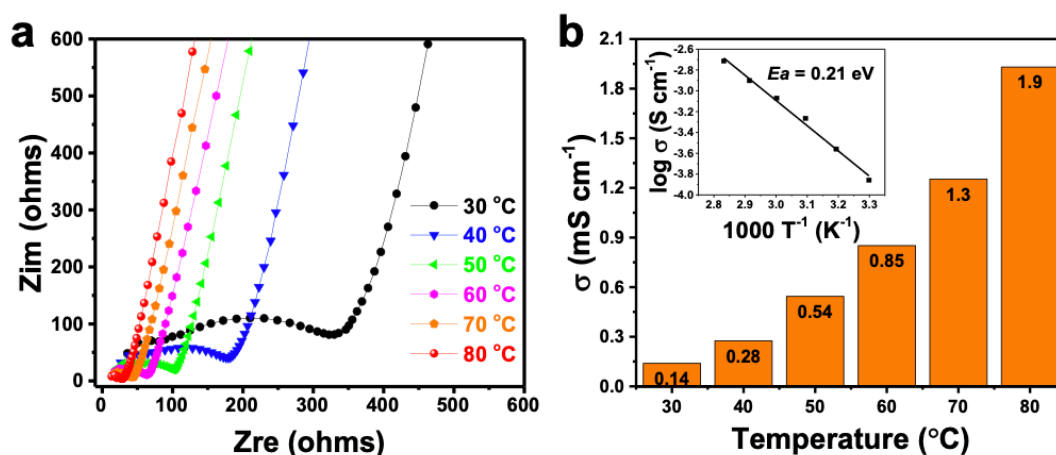

Figure 4. Nyquist plots of the LATP-Li$_3$InCl$_6$·nDMF composite electrolyte measured at different temperatures (**a**), and the corresponding ionic conductivities (**b**).

The ionic conductivity of the fabricated composite electrolyte was measured at different temperatures (Figure 4a). The Nyquist plots show that the semi-circles decrease in size with increasing testing temperatures. Figure 4b, presents the ionic conductivity values obtained at different temperatures after equivalent circuit fitting. The conductivity was found to be 0.14 mS cm^{-1} at 30 °C and 1.9 mS cm^{-1} at 80 °C. The activation energy of the composite electrolyte was calculated to be 0.21 eV based on the Arrhenius equation [47], which is lower than that of pure LATP bulk electrolyte [48].

The cold-sintered LATP-Li$_3$InCl$_6$·nDMF composite SSE was assembled into a symmetric Li|LATP-Li$_3$InCl$_6$·nDMF|Li cell, demonstrating the plating/stripping process at 55 ℃ and 100 ℃ (Figure 5). In the first several cycles (Figure S3), the

symmetric cell was tested under various current densities of 0.02, 0.05, 0.1, 0.2, 0.5, 1 mA cm^{-2}, and back to 0.1 mA cm^{-2} at the temperature of 55 ℃. The voltage was kept under 0.35 V when the current density increased up to 1 mA cm^{-2}. When the current density recovered back to 0.1 mA cm^{-2}, the cell voltage move from 0.05 V and gradually increased to 0.15 V when cycled over 1600 hours, showing good cycling stability with a long cycling life (Figure 5a). Furthermore, the cell was tested under the current density of 1 mA cm^{-2} at a high temperature of 100 ℃ (Figure 5b). The cell exhibited an overpotential of around 0.03V for the first hour and keep decreasing to 0.012V for the 600th hour and to around 0.01 V for the 1200th hour showing a stable cycling performance at high temperature, consistent with the high conductivity of the composite electrolyte and low activation energy.
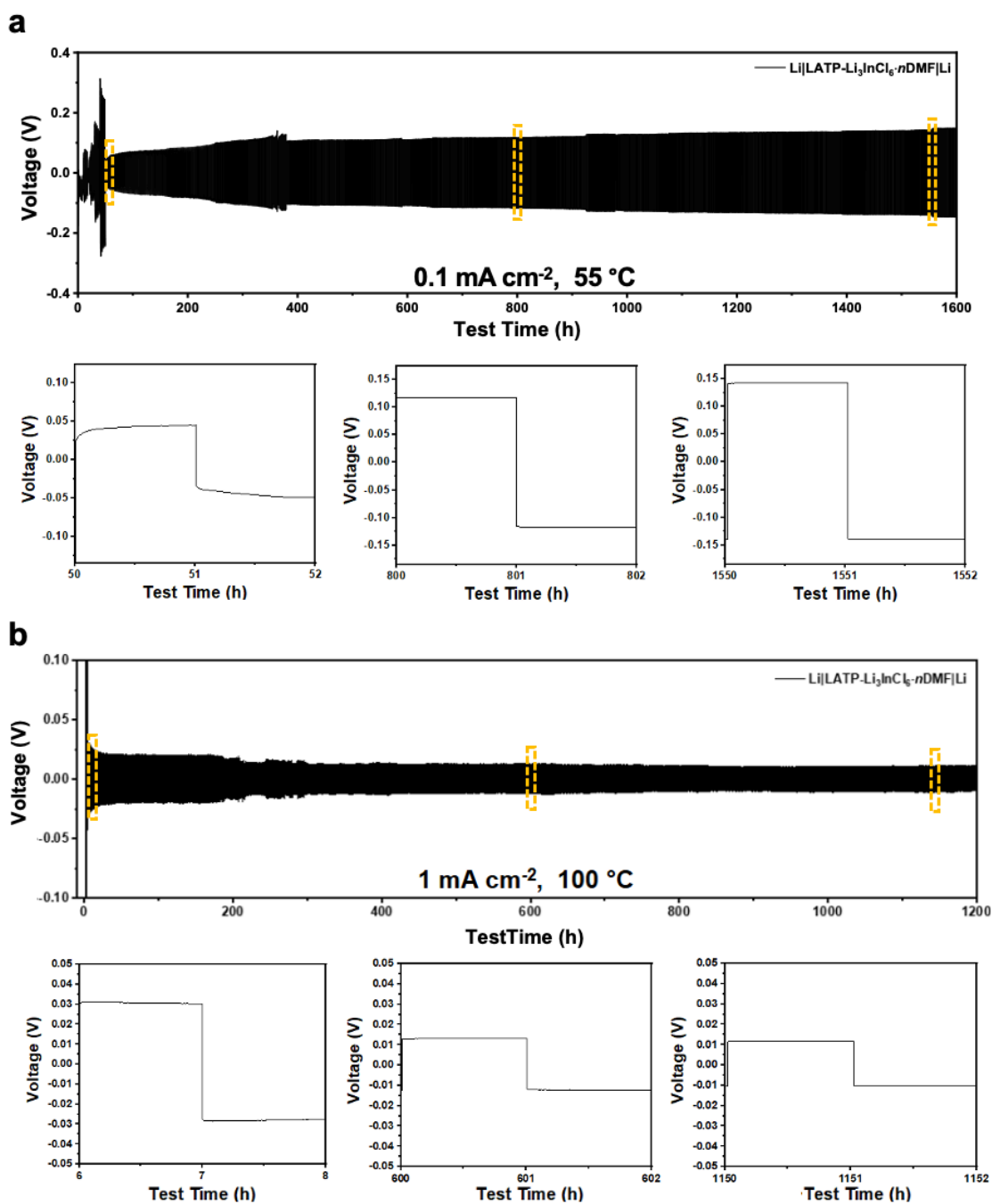
Figure 5. Galvanostatic cycling of symmetric Li|LATP-Li$_3$InCl$_6$·nDMF|Li cell. The voltage profile for the lithium plating/stripping cycling at (**a**) 0.1 mA cm^{-2}, 55 ℃ and (**b**) 1.0 mA cm^{-2}, 100 ℃.

Conclusion

In this work, the LATP-Li$_3$InCl$_6$·nDMF ceramic-ceramic composite electrolyte was successfully fabricated using the cold sintering process. The halide phase, Li$_3$InCl$_6$·nDMF, precipitated as a boundary phase, effectively bridging the LATP

particles with the assistance of a transient liquid (DMF), thereby enhancing Li^+ conduction in the composite SSEs. The influence of DMF as a transient liquid on the densification process and composite structure was investigated to improve ionic conductivity across interfacial boundaries. Consequently, the composite electrolyte exhibited an ionic conductivity of 1.4×10^{-4} S cm^{-1} at room temperature. The composite electrolyte demonstrated effective dendrite blocking, evidenced by stable lithium stripping/plating for over a thousand hours at 55 and 100 °C in a symmetric Li| LATP-Li$_3$InCl$_6 \cdot n$DMF |Li cell. The low overpotential (*e.g.*, 0.018 V at 100 °C) aligns with the small activation energy and high ionic conductivity at elevated temperatures. Therefore, the cold sintered LATP-Li$_3$InCl$_6 \cdot n$DMF composite electrolyte represents the first demonstration of ceramic-in-ceramic SSEs that combine the advantages of oxides and halides, impacting the development of high-performance lithium metal all-solid-state batteries, especially at extreme temperatures.

Declaration of Competing interests

The authors declare no competing financial interests.

Acknowledgements

Appendix. Supporting materials

Supplementary information is available in the online version of the paper.

References

(1)   Cano, Z. P.; Banham, D.; Ye, S.; Hintennach, A.; Lu, J.; Fowler, M.; Chen, Z. Batteries and Fuel Cells for Emerging Electric Vehicle Markets. *Nat. Energy* **2018**, *3* (4), 279–289. https://doi.org/10.1038/s41560-018-0108-1.

(2)   Forsyth, M.; Porcarelli, L.; Wang, X.; Goujon, N.; Mecerreyes, D. Innovative Electrolytes Based on Ionic Liquids and Polymers for Next-Generation Solid-State Batteries. *Acc. Chem. Res.* **2019**, *52* (3), 686–694. https://doi.org/10.1021/acs.accounts.8b00566.

(3)   Kim, J.; Kwon, K.; Kim, K.; Han, S.; Kim, P. J.; Choi, J. Size Effect of a Piezoelectric Material as a Separator Coating Layer for Suppressing Dendritic Li Growth in Li Metal Batteries. *Nanomaterials* **2023**, *13* (1), 1–10. https://doi.org/10.3390/nano13010090.

(4)   Ding, F.; Xu, W.; Graff, G. L.; Zhang, J.; Sushko, M. L.; Chen, X.; Shao, Y.; Engelhard, M. H.; Nie, Z.; Xiao, J.; Liu, X.; Sushko, P. V.; Liu, J.; Zhang, J. G. Dendrite-Free Lithium Deposition via Self-Healing Electrostatic Shield Mechanism. *J. Am. Chem. Soc.* **2013**, *135* (11), 4450–4456. https://doi.org/10.1021/ja312241y.

(5)   Feng, J.; Wang, L.; Chen, Y.; Wang, P.; Zhang, H.; He, X. PEO Based Polymer-Ceramic Hybrid Solid Electrolytes: A Review. *Nano Converg.* **2021**, *8* (1). https://doi.org/10.1186/s40580-020-00252-5.

(6)   Yu, X.; Jiang, Z.; Yuan, R.; Song, H. A Review of the Relationship between Gel Polymer Electrolytes and Solid Electrolyte Interfaces in Lithium Metal Batteries. *Nanomaterials* **2023**, *13* (11). https://doi.org/10.3390/nano13111789.

(7)   Qian, J.; Henderson, W. A.; Xu, W.; Bhattacharya, P.; Engelhard, M.; Borodin, O.; Zhang, J. G. High Rate and Stable Cycling of Lithium Metal Anode. *Nat. Commun.* **2015**, *6*. https://doi.org/10.1038/ncomms7362.

(8)   Manthiram, A.; Yu, X.; Wang, S. Lithium Battery Chemistries Enabled by Solid-State Electrolytes. *Nat. Rev. Mater.* **2017**, *2* (4), 1–16. https://doi.org/10.1038/natrevmats.2016.103.

(9)   Nie, B.; Liu, T.; Alcoutlabi, M.; Basu, S.; Kumara, S.; Li, M.; Lian, J.; Sun, H. Cold Sintering-Enabled Interface Engineering of Composites for Solid-State Batteries. *Front. Energy Res.* **2023**, *11* (February), 1–7. https://doi.org/10.3389/fenrg.2023.1149103.

(10)   Sun, C.; Liu, J.; Gong, Y.; Wilkinson, D. P.; Zhang, J. Recent Advances in All-Solid-State Rechargeable Lithium Batteries. *Nano Energy* **2017**, *33* (December 2016), 363–386. https://doi.org/10.1016/j.nanoen.2017.01.028.

(11)   Ramasubramanian, B.; Reddy, M. V.; Zaghib, K.; Armand, M.; Ramakrishna, S. Growth Mechanism of Micro/Nano Metal Dendrites and Cumulative Strategies for Countering Its Impacts in Metal Ion Batteries: A Review†. *Nanomaterials* **2021**, *11* (10). https://doi.org/10.3390/nano11102476.

(12)   Bang, S. H.; Tsuji, K.; Ndayishimiye, A.; Dursun, S.; Seo, J. H.; Otieno, S.; Randall, C. A. Toward a Size Scale-up Cold Sintering Process at Reduced

Uniaxial Pressure. *J. Am. Ceram. Soc.* **2020**, *103* (4), 2322–2327. https://doi.org/10.1111/jace.16976.

(13)   Hamao, N.; Yamaguchi, Y.; Hamamoto, K. Densification of a NASICON-Type LATP Electrolyte Sheet by a Cold-Sintering Process. *Materials (Basel).* **2021**, *14* (16). https://doi.org/10.3390/ma14164737.

(14)   Grady, Z.; Fan, Z.; Ndayishimiye, A.; Randall, C. A. Design and Sintering of All-Solid-State Composite Cathodes with Tunable Mixed Conduction Properties via the Cold Sintering Process. *ACS Appl. Mater. Interfaces* **2021**, *13* (40), 48071–48087. https://doi.org/10.1021/acsami.1c13913.

(15)   Sharafi, A.; Kazyak, E.; Davis, A. L.; Yu, S.; Thompson, T.; Siegel, D. J.; Dasgupta, N. P.; Sakamoto, J. Surface Chemistry Mechanism of Ultra-Low Interfacial Resistance in the Solid-State Electrolyte Li7La3Zr2O12. *Chem. Mater.* **2017**, *29* (18), 7961–7968. https://doi.org/10.1021/acs.chemmater.7b03002.

(16)   Liu, C.; Deng, L.; Li, X.; Wu, T.; Zhang, W.; Cui, H.; Yang, H. Metal–Organic Frameworks for Solid-State Electrolytes: A Mini Review. *Electrochem. commun.* **2023**, *150* (April), 107491. https://doi.org/10.1016/j.elecom.2023.107491.

(17)   Famprikis, T.; Canepa, P.; Dawson, J. A.; Islam, M. S.; Masquelier, C. Fundamentals of Inorganic Solid-State Electrolytes for Batteries. *Nat. Mater.* **2019**, *18* (12), 1278–1291. https://doi.org/10.1038/s41563-019-0431-3.

(18)   Zheng, Y.; Yao, Y.; Ou, J.; Li, M.; Luo, D.; Dou, H.; Li, Z.; Amine, K.; Yu, A.; Chen, Z. A Review of Composite Solid-State Electrolytes for Lithium Batteries: Fundamentals, Key Materials and Advanced Structures. *Chem. Soc. Rev.* **2020**, *49* (23), 8790–8839. https://doi.org/10.1039/d0cs00305k.

(19)   Okumura, T.; Taminato, S.; Miyazaki, Y.; Kitamura, M.; Saito, T.; Takeuchi, T.; Kobayashi, H. LISICON-Based Amorphous Oxide for Bulk-Type All-Solid-State Lithium-Ion Battery. *ACS Appl. Energy Mater.* **2020**, *3* (4), 3220–3229. https://doi.org/10.1021/acsaem.9b01949.

(20)   Zheng, F.; Kotobuki, M.; Song, S.; Lai, M. O.; Lu, L. Review on Solid Electrolytes for All-Solid-State Lithium-Ion Batteries. *J. Power Sources* **2018**, *389* (February), 198–213. https://doi.org/10.1016/j.jpowsour.2018.04.022.

(21)   Meesala, Y.; Jena, A.; Chang, H.; Liu, R. S. *Recent Advancements in Li-Ion Conductors for All-Solid-State Li-Ion Batteries*; 2017; Vol. 2.

https://doi.org/10.1021/acsenergylett.7b00849.

(22) Ren, Y.; Chen, K.; Chen, R.; Liu, T.; Zhang, Y.; Nan, C. W. Oxide Electrolytes for Lithium Batteries. *J. Am. Ceram. Soc.* **2015**, *98* (12), 3603–3623. https://doi.org/10.1111/jace.13844.

(23) Yang, K.; Chen, L.; Ma, J.; He, Y.; Kang, F. Progress and Perspective of Li 1 + x Al x Ti 2 -x (PO 4) 3 Ceramic Electrolyte in Lithium Batteries . *InfoMat* **2021**, *3* (11), 1195–1217. https://doi.org/10.1002/inf2.12222.

(24) Dias, J. A.; Santagneli, S. H.; Messaddeq, Y. Methods for Lithium Ion NASICON Preparation: From Solid-State Synthesis to Highly Conductive Glass-Ceramics. *J. Phys. Chem. C* **2020**, *124* (49), 26518–26539. https://doi.org/10.1021/acs.jpcc.0c07385.

(25) Li, C.; Li, R.; Liu, K.; Si, R.; Zhang, Z.; Hu, Y. NaSICON: A Promising Solid Electrolyte for Solid-state Sodium Batteries. *Interdiscip. Mater.* **2022**, *1* (3), 396–416. https://doi.org/10.1002/idm2.12044.

(26) Inada, R.; Takeda, A.; Yamazaki, Y.; Miyake, S.; Sakurai, Y.; Thangadurai, V. Effect of Postannealing on the Properties of a Ta-Doped Li7La3Zr2O12Solid Electrolyte Degraded by Li Dendrite Penetration. *ACS Appl. Energy Mater.* **2020**, *3* (12), 12517–12524. https://doi.org/10.1021/acsaem.0c02474.

(27) Liu, Y.; Liu, J.; Sun, Q.; Wang, D.; Adair, K. R.; Liang, J.; Zhang, C.; Zhang, L.; Lu, S.; Huang, H.; Song, X.; Sun, X. Insight into the Microstructure and Ionic Conductivity of Cold Sintered NASICON Solid Electrolyte for Solid-State Batteries. *ACS Appl. Mater. Interfaces* **2019**, *11* (31), 27890–27896. https://doi.org/10.1021/acsami.9b08132.

(28) Nie, B.; Sun, H. Probing Cold Sintering-Regulated Interfaces and Integration of Polymer-in-Ceramic Solid-State Electrolytes. 1–19.

(29) Epp, V.; Ma, Q.; Hammer, E. M.; Tietz, F.; Wilkening, M. Very Fast Bulk Li Ion Diffusivity in Crystalline Li1.5Al0.5Ti1.5(PO4)3 as Seen Using NMR Relaxometry. *Phys. Chem. Chem. Phys.* **2015**, *17* (48), 32115–32121. https://doi.org/10.1039/c5cp05337d.

(30) Wang, S.; Ding, Y.; Zhou, G.; Yu, G.; Manthiram, A. Durability of the Li1+xTi2-XAlx(PO4)3 Solid Electrolyte in Lithium-Sulfur Batteries. *ACS Energy Lett.* **2016**, *1* (6), 1080–1085. https://doi.org/10.1021/acsenergylett.6b00481.

(31) Nagata, K.; Nanno, T. All Solid Battery with Phosphate Compounds Made

through Sintering Process. *J. Power Sources* **2007**, *174* (2), 832–837. https://doi.org/10.1016/j.jpowsour.2007.06.227.

(32) Arbi, K.; Bucheli, W.; Jiménez, R.; Sanz, J. High Lithium Ion Conducting Solid Electrolytes Based on NASICON Li1+xAlxM2-x(PO4)3 Materials (M = Ti, Ge and 0 ≤ x ≤ 0.5). *J. Eur. Ceram. Soc.* **2015**, *35* (5), 1477–1484. https://doi.org/10.1016/j.jeurceramsoc.2014.11.023.

(33) Yan, G.; Yu, S.; Nonemacher, J. F.; Tempel, H.; Kungl, H.; Malzbender, J.; Eichel, R. A.; Krüger, M. Influence of Sintering Temperature on Conductivity and Mechanical Behavior of the Solid Electrolyte LATP. *Ceram. Int.* **2019**, *45* (12), 14697–14703. https://doi.org/10.1016/j.ceramint.2019.04.191.

(34) Duan, S.; Jin, H.; Yu, J.; Esfahani, E. N.; Yang, B.; Liu, J.; Ren, Y.; Chen, Y.; Lu, L.; Tian, X.; Hou, S.; Li, J. Non-Equilibrium Microstructure of Li1.4Al0.4Ti1.6(PO4)3 Superionic Conductor by Spark Plasma Sintering for Enhanced Ionic Conductivity. *Nano Energy* **2018**, *51* (June), 19–25. https://doi.org/10.1016/j.nanoen.2018.06.050.

(35) Yi, E. jeong; Yoon, K. young; Jung, H. A.; Nakayama, T.; Ji, M. jung; Hwang, H. Fabrication and Electrochemical Properties of Li 1.3 Al 0.3 Ti 1.7 (PO 4) 3 Solid Electrolytes by Sol-Gel Method. *Appl. Surf. Sci.* **2019**, *473* (September 2018), 622–626. https://doi.org/10.1016/j.apsusc.2018.12.202.

(36) Duluard, S.; Paillassa, A.; Puech, L.; Vinatier, P.; Turq, V.; Rozier, P.; Lenormand, P.; Taberna, P. L.; Simon, P.; Ansart, F. Lithium Conducting Solid Electrolyte Li1.3Al0.3Ti1.7(PO4)3 Obtained via Solution Chemistry. *J. Eur. Ceram. Soc.* **2013**, *33* (6), 1145–1153. https://doi.org/10.1016/j.jeurceramsoc.2012.08.005.

(37) Duluard, S.; Paillassa, A.; Lenormand, P.; Taberna, P. L.; Simon, P.; Rozier, P.; Ansart, F. Dense on Porous Solid LATP Electrolyte System: Preparation and Conductivity Measurement. *J. Am. Ceram. Soc.* **2017**, *100* (1), 141–149. https://doi.org/10.1111/jace.14451.

(38) Guo, J.; Guo, H.; Baker, A. L.; Lanagan, M. T.; Kupp, E. R.; Messing, G. L.; Randall, C. A. Cold Sintering: A Paradigm Shift for Processing and Integration of Ceramics. *Angew. Chemie - Int. Ed.* **2016**, *55* (38), 11457–11461. https://doi.org/10.1002/anie.201605443.

(39) Jiang, P.; Guo, P.; Shi, Y.; Li, S.; Li, K.; Lu, X. Y.; Zhang, Z.; He, D.; Bian, J.; Lu, X. Solid-State Li Metal Battery Enabled by Cold Sintering at 120 °C. *Mater. Today Phys.* **2021**, *20*. https://doi.org/10.1016/j.mtphys.2021.100476.

(40)   Kim, S.; Gim, Y.; Lee, W. Thermally Stable Ceramic-Salt Electrolytes for Li Metal Batteries Produced from Cold Sintering Using DMF/Water Mixture Solvents. *Nanomaterials* **2023**, *13* (17). https://doi.org/10.3390/nano13172436.

(41)   Ferrer-Nicomedes, S.; Mormeneo-Segarra, A.; Vicente-Agut, N.; Barba-Juan, A. Introducing an Ionic Conductive Matrix to the Cold-Sintered Li1.3Al0.3Ti1.7(PO4)3-Based Composite Solid Electrolyte to Enhance the Electrical Properties. *J. Power Sources* **2023**, *581* (June). https://doi.org/10.1016/j.jpowsour.2023.233494.

(42)   Berbano, S. S.; Guo, J.; Guo, H.; Lanagan, M. T.; Randall, C. A. Cold Sintering Process of Li1.5Al0.5Ge1.5(PO4)3 Solid Electrolyte. *J. Am. Ceram. Soc.* **2017**, *100* (5), 2123–2135. https://doi.org/10.1111/jace.14727.

(43)   Tatebe, C. J.; Yusuf, S.; Bellas, M. K.; Zeller, M.; Arntsen, C.; Genna, D. T. On the Role of Dioxane in the Synthesis of In-Derived MOFs. *Cryst. Growth Des.* **2021**, *21* (12), 6840–6846. https://doi.org/10.1021/acs.cgd.1c00766.

(44)   Sada, T.; Ndayishimiye, A.; Fan, Z.; Fujioka, Y.; Randall, C. A. Surface Modification of BaTiO3 with Catechol Surfactant and Effects on Cold Sintering. *J. Appl. Phys.* **2021**, *129* (18). https://doi.org/10.1063/5.0049905.

(45)   Heravi, M. M.; Ghavidel, M.; Mohammadkhani, L. Beyond a Solvent: Triple Roles of Dimethylformamide in Organic Chemistry. *RSC Adv.* **2018**, *8* (49), 27832–27862. https://doi.org/10.1039/c8ra04985h.

(46)   Mormeneo-Segarra, A.; Ferrer-Nicomedes, S.; Vicente-Agut, N.; Barba-Juan, A. In Operando Characterization of the Ionic Conductivity Dependence on Liquid Transient Phase and Microstructure of Cold-Sintered Bi2O3-Doped Li1.3Al0.3Ti1.7(PO4)3 Solid-State Electrolyte. *Ceram. Int.* **2023**, *49* (22), 36497–36506. https://doi.org/10.1016/j.ceramint.2023.08.333.

(47)   Petrowsky, M.; Frech, R. Temperature Dependence of Ion Transport: The Compensated Arrhenius Equation. *J. Phys. Chem. B* **2009**, *113* (17), 5996–6000. https://doi.org/10.1021/jp810095g.

(48)   Rosen, M.; Hecker, P.; Mann, M.; Ma, Q.; Gross, J. P.; Schwaiger, R.; Guillon, O.; Fattakhova-Rohlfing, D.; Finsterbusch, M. Reducing the Environmental Footprint of Solid-Electrolytes - a Green Synthesis Route for LATP. *Green Chem.* **2024**, *26* (5), 2712–2720. https://doi.org/10.1039/d3gc03293k.